Int. J. Solids Structures Vol. 27, No. 7, pp. 849–864, 1991
Printed in Great Britain.

0020-7683/91 $3.00+.00
© 1990 Pergamon Press plc

ANALYSIS OF A ZIG-ZAG ARRAY OF CIRCULAR HOLES IN AN INFINITE SOLID UNDER UNIAXIAL TENSION

M. ISIDA and H. IGAWA
Department of Mechanical Engineering, Kurume Institute of Technology, 2228 Kamitsu-machi, Kurume 830, Japan

(*Received* 29 *March* 1989; *in revised form* 27 *February* 1990)

Abstract—This paper is concerned with a theoretical analysis of an infinite zig-zag array of circular holes in an infinite solid under uniaxial tension. We use properly defined unit regions, assume complex stress potentials in the form of Laurent series expansions and determine the unknown coefficients from the boundary conditions for the unit regions used. Numerical results for the maximum stress, the stress concentration factor and the effect of perforation on the tensile stiffness of the solid are given for various hole sizes and hole spacings in both directions. The results are fitted to reliable polynomial formulae for convenience in engineering applications.

1. INTRODUCTION

A zig-zag array of circular holes is quite important, not only as a basic stress concentration problem, but also as a model of randomly distributed voids in materials. This problem was treated by Saito (1957) and Bailey and Hicks (1960), but their analyses were confined to a square array of holes, and the maximum stress was arbitrarily assumed to occur across the ligament. In the present paper, we analyze general zig-zag arrays of circular holes in an infinite solid under uniaxial tension, and examine the effects of the size and the relative location of the holes on the maximum stress and the apparent tensile stiffness of the solid.

In the analysis, we choose suitable unit regions, and assume Laurent series expansions for the complex potentials in forms satisfying the traction-free conditions along the hole edges. Then the unknown coefficients in the Laurent series are determined from the boundary conditions at the outer edges of the unit regions used. At this stage, we use a new procedure based on element-wise resultant forces and displacements in order to get highly accurate results. This method was developed by Isida (1971), and proved a powerful technique both in plane problems (Isida, 1978; Isida and Nemat-Nasser, 1987), and three-dimensional problems (Isida *et al.*, 1983, 1984; Isida and Noguchi, 1984).

Numerical calculations are carried out for various hole sizes and hole spacings in both directions. The results for the maximum stress, the stress concentration factor and the tensile stiffness of the perforated solid are represented in tables and figures. These results are then fitted to reliable polynomial formulae for convenience in engineering applications.

2. THEORETICAL ANALYSIS

2.1. *Fundamental equations and description of problem*

In plane elasticity, all the physical quantities are given in terms of two complex potentials $\phi(z)$, $\psi(z)$ and their derivatives, where $z = x+iy$ (Timoshenko and Goodier, 1951).

Components of stress:

$$\sigma_y+\sigma_x = 4\,\mathrm{Re}\,[\phi'(z)] \tag{1a}$$

$$\sigma_y-\sigma_x+2i\tau_{xy} = 2[\bar{z}\phi''(z)+\psi'(z)]. \tag{1b}$$

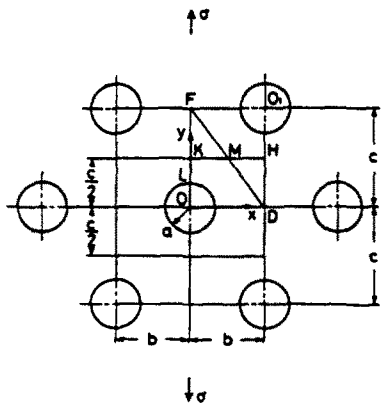

Fig. 1. Doubly-periodic zig-zag array of circular holes in an infinite solid subjected to tension.

Components of resultant force:

$$P_y + iP_x = -\bar{\phi}(\bar{z}) - z\phi'(z) - \psi(z) + (\text{an arbitrary constant}). \tag{2}$$

Components of displacement:

$$2G(u - iv) = \kappa\bar{\phi}(\bar{z}) - z\phi'(z) - \psi(z) + (\text{an arbitrary constant}) \tag{3}$$

where G is the shear modulus, and κ is defined by Poisson's ratio ν as

$$\kappa = \begin{cases} \dfrac{3-\nu}{1+\nu} & \text{(plane stress)} \\ 3-4\nu & \text{(plane strain).} \end{cases} \tag{4}$$

Constant terms in eqns (2) and (3) depend on the starting points from which P_y, P_x and u, v are measured, but they are not essential in the analysis.

We also have the following expressions for the stresses in polar coordinates:

$$\sigma_\theta + \sigma_r = 4\,\mathrm{Re}\,[\phi'(z)] \tag{5a}$$

$$\sigma_\theta - \sigma_r + 2i\tau_{r\theta} = 2\,e^{2i\theta}\,[\bar{z}\phi''(z) + \psi'(z)]. \tag{5b}$$

This paper deals with an infinite solid containing an infinite zig-zag array of circular holes. Let the radius of the holes be a, and the spacings between adjacent holes in horizontal and vertical rows be $2b$ and $2c$, respectively, as shown in Fig. 1. The x- and y-axes are taken with their origin at the center of one of the holes, and the solid is subjected to an average tensile stress σ in the y-direction. Figures 10(a) and (b) of Section 3.3.3 show the two typical arrays of holes corresponding to $c/b = 1$ and $\sqrt{3}$, which are the square array and the equilateral triangular array, respectively.

2.2. *Laurent series expansions of complex stress potentials*

We take proper unit regions and express the complex stress potentials in forms satisfying the symmetry conditions as well as the traction-free conditions along the hole edges. We then determine the unknown coefficients in the stress potentials from the boundary conditions at the outer edges of the unit regions.

For the above unit regions, we have chosen the triangle ODF and the rectangle ODHK shown in Fig. 1, noting the symmetry of the stress field about both the coordinates' axes. Usually the triangular region is more simple and convenient to use than the rectangular region, but the latter is also used for large values of c/b since the triangular region gives poor results.

The complex potentials $\phi(z)$ and $\psi(z)$ must be analytic in the unit region, and they can be expanded in the following Laurent series:

$$\phi(z) = \sum_{n=0}^{\infty} (K_{2n} z^{2n+1} + F_{2n} z^{-2n-1}) \tag{6a}$$

$$\psi(z) = \sum_{n=0}^{\infty} (L_{2n} z^{2n+1} + H_{2n} z^{-2n-1}). \tag{6b}$$

Note that symmetry dictates that all of the even power terms are missing, and that all of the coefficients are real in both the above expressions.

The hole edge must be traction-free, or $\sigma_r = \tau_{r\theta} = 0$. We then subtract (5b) from (5a), use eqns (6) with $z = a\,e^{i\theta}$ and express $(\sigma_r - i\tau_{r\theta})_{r=a}$ in power series of $e^{i\theta}$. Equating all the coefficients to zero, we get the following relations among the coefficients in eqns (6):

$$H_0 = -2a^2 K_0, \quad H_{2n} = -(2n)^2 a^{4n+2} K_{2n} - (2n-1) a^{4n} L_{2n-2} \quad (n \geqslant 1) \tag{7a}$$

$$F_{2n-2} = -(2n+1) a^{4n} K_{2n} - a^{4n-2} L_{2n-2} \quad (n \geqslant 1). \tag{7b}$$

Inserting eqns (7) into eqns (6), $\phi(z)$ and $\psi(z)$ are reduced to the forms containing independent unknown coefficients K_{2n} and L_{2n}.

2.3. *Boundary conditions and determination of unknowns*

The complex potentials (6), rewritten in terms of the independent unknowns K_{2n} and L_{2n} using eqns (7), completely satisfy the traction-free conditions along the hole edge, as well as symmetry conditions. Therefore, the unknowns K_{2n} and L_{2n} must be determined only from the boundary conditions along the outer edges of the unit regions used: along the side DF for the triangular region, or along the sides DH and HK for the rectangular region.

For the numerical calculation, we use a method based on element-wise resultant forces and displacements. This method was developed by Isida (1971) and proved a powerful technique in analyzing various problems of multi-connected regions (Isida, 1978; Isida *et al.*, 1983, 1984; Isida and Noguchi, 1984; Isida and Nemat-Nasser, 1987). The procedure will be described below for each of the unit regions.

(a) *Triangular unit region* [Fig. 2(a)]. Let M be the mid-point of the side DF, and let S_1 and S_2 denote the two points on this side equally distant from the point M. Then the points S_1 and S_2 should be in the same stress state and the displacements of these points relative to M should be the same.

In order to take advantage of these conditions in numerical computations, we divide the side DF into N equal intervals $Q_1Q_2, Q_2Q_3, \ldots, Q_NQ_{N+1}$, where N is an even integer, $N = 2m$ [see Fig. 2(a)].

First, the two points Q_t and Q_{2m+2-t} $(t = 1, 2, \ldots, m)$, which are equally distant from the point M, should be in the same stress state. This requires the following conditions on the resultant forces:

$$[P_x]_{Q_t}^{Q_{m+1}} = [P_x]_{Q_{m+1}}^{Q_{2m+2-t}} \tag{8a}$$

$$[P_y]_{Q_t}^{Q_{m+1}} = [P_y]_{Q_{m+1}}^{Q_{2m+2-t}} \quad (t = 1, 2, \ldots, m;\ m = N/2) \tag{8b}$$

where $[\ ]_A^B$ denotes the difference of the values of the quantity within the brackets at points B and A.

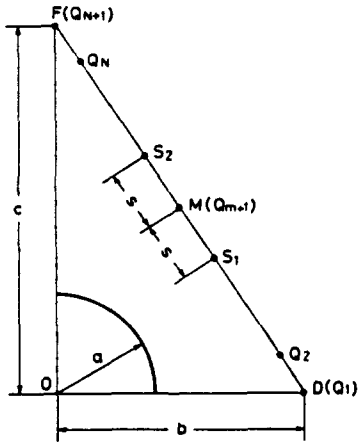

Fig. 2(a). Triangular unit region.

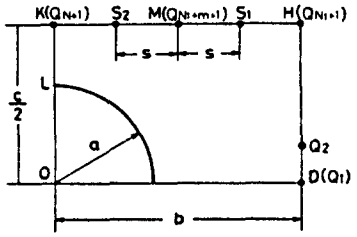

Fig. 2(b). Rectangular unit region.

Secondly, the equality of the displacements at Q_t and Q_{2m+2-t} relative to M requires that

$$[u]_t^{m+1} = [u]_{m+1}^{2m+2-t} \tag{9a}$$

$$[v]_t^{m+1} = [v]_{m+1}^{2m+2-t} \quad (t = 1, 2, \ldots, m; m = N/2). \tag{9b}$$

Furthermore, the resultant forces along the side DF should balance the external load,

$$[P_x]_D^F = 0, \quad [P_y]_D^F = \sigma b. \tag{10}$$

Equations (8)–(10) give $(2N+2)$ relations to determine the unknown coefficients K_{2n} and L_{2n}.

(b) *Rectangular unit region* [Fig. 2(b)]. We divide the sides DH and HK into N_1 and N_2 equal intervals, respectively, where N_2 is taken to be an even integer, $N_2 = 2m$. These intervals are Q_1Q_2, Q_2Q_3, ... and Q_NQ_{N+1} $(N = N_1 + N_2)$, as shown in Fig. 2(b).

The stress state is symmetric about DH, that is: $\tau_{xy} = 0$ and u = constant along DH. These conditions are replaced by the following relations in terms of P_y and u for each of the intervals:

$$[P_y]_j = 0 \quad (j = 1, 2, \ldots, N_1) \tag{11a}$$

$$[u]_{j+1} - [u]_j = 0 \quad (j = 1, 2, \ldots, N_1 - 1) \tag{11b}$$

where j is the interval number. $[P_y]_j$ in eqns (11) is determined from the real part of eqn (2) by taking the difference in the values at the two points Q_{j+1} and Q_j, and $[u]_j$ is defined by the mean of u at Q_{j+1} and Q_j as obtained from the real part of eqn (3).

$$[P_y]_j = P_{y,Q_{j+1}} - P_{y,Q_j} \tag{12a}$$

$$[u]_j = (u_{Q_{j+1}} + u_{Q_j})/2 \quad (j = 1, 2, \ldots, N_1). \tag{12b}$$

The boundary conditions along the side HK can be processed in a manner similar to that for the side DF for the triangular unit region. Let M be the mid-point of HK. Then the two points S_1 and S_2 on HK equally distant from M must be in the same stress state, and the displacements at S_1 and S_2 relative to M must be the same. These boundary conditions lead to the following relations:

$$[P_x]_{Q_{N_1+t}}^{Q_{N_1+m+1}} = [P_x]_{Q_{N_1+m+1}}^{Q_{N_1+2m+2-t}} \tag{13a}$$

$$[P_y]_{Q_{N_1+t}}^{Q_{N_1+m+1}} = [P_y]_{Q_{N_1+m+1}}^{Q_{N_1+2m+2-t}} \quad (t = 1, 2, \ldots, m; m = N_2/2) \tag{13b}$$

$$[u]_{Q_{N_1+t}}^{Q_{N_1+m+1}} = [u]_{Q_{N_1+m+1}}^{Q_{N_1+2m+2-t}} \tag{14a}$$

$$[v]_{Q_{N_1+t}}^{Q_{N_1+m+1}} = [v]_{Q_{N_1+m+1}}^{Q_{N_1+2m+2-t}} \quad (t = 1, 2, \ldots, m; m = N_2/2). \tag{14b}$$

Furthermore, the resultant forces acting along the outer edges of this region should balance the external load, and we have

$$[P_x]_D^H + [P_x]_K^L = 0, \quad [P_y]_H^K = \sigma b. \tag{15}$$

Thus the boundary conditions for the rectangular unit region are replaced by $(2N+1)$ relations consisting of eqns (11) and (13)–(15), where $N = N_1 + N_2$.

As shown above, we have $(2N+2)$ and $(2N+1)$ boundary relations for the triangular and rectangular unit regions, respectively. Corresponding to these relations, we take $(2N+2)$ unknowns K_{2n}, L_{2n} $(n = 0, 1, 2, \ldots, N)$ for the triangular region, and $(2N+1)$ unknowns K_{2n} $(n = 0, 1, 2, \ldots, N)$, L_{2n} $(n = 0, 1, 2, \ldots, N-1)$ for the rectangular region, neglecting higher order coefficients. These unknowns are determined by the corresponding boundary conditions.

3. NUMERICAL RESULTS

3.1. *General remarks on numerical analysis and accuracy of results*

The numerical results of this problem depend upon the ratio of a, b and c, or upon the two dimensionless parameters

$$\mu = \frac{b}{c}, \quad \lambda = \frac{a}{b}. \tag{16}$$

We also define the following parameters:

$$\lambda_1 = \frac{a}{c} = \lambda\mu \tag{17}$$

$$f = \text{porosity} = \frac{\pi a^2}{2bc} = \frac{\pi}{2}\lambda^2\mu \tag{18}$$

where the porosity f is the volume fraction of the holes used in specifying the tensile stiffness of the porous solid.

In the present problem, we are especially interested in two quantities. One is the maximum circumferential stress, and the other is the effect of holes on the apparent tensile stiffness of the solid. With reference to the latter quantity, the following dimensionless factor C is defined:

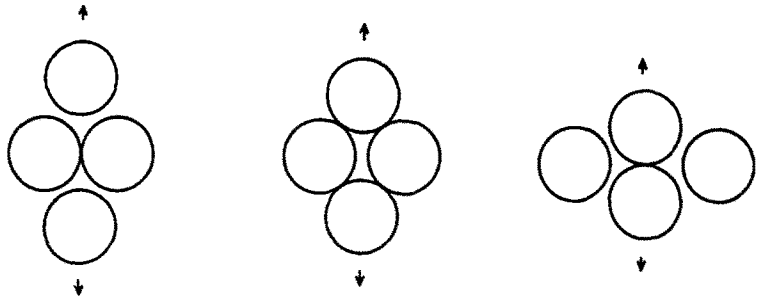

Fig. 3. Three extreme cases when adjacent holes touch each other.

$$C = \frac{E^*}{E_0} = \text{tensile stiffness factor} \tag{19a}$$

$$E^* = \text{apparent Young's modulus of solid with holes} \tag{19b}$$

$$E_0 = \text{Young's modulus of material} = \begin{cases} E/(1-\nu^2) & \text{(plane strain)} \\ E & \text{(plane stress).} \end{cases} \tag{19c}$$

E is Young's modulus of the material measured with thin plate specimens. E_0 and E^* depend on E and ν, but $C = E^*/E_0$ is independent of them and is common to the plane stress and the plane strain cases.

Numerical calculations have been carried out for 138 combinations of μ and λ as shown in Table 3 of Section 3.3.1, where the upper limit of λ evidently depends on μ. Obviously, λ cannot exceed the values for the extreme cases when some of the adjacent holes touch each other, as shown in Fig. 3(a–c), depending on the three ranges of μ. This physical upper limit of λ is given as a function of μ in each of the above three ranges of μ, and is shown by the kinked dashed curve in Fig. 4. The practical upper limit on λ is given below for which the present analysis gives reliable results with reasonable computing cost. This has been found to be about 80% of the physical limit,

$$\lambda \leqslant \begin{cases} 0.8 & (\mu \leqslant 1/\sqrt{3}) \\ 0.8\sqrt{1+\mu^2}/(2\mu) & (1/\sqrt{3} \leqslant \mu \leqslant \sqrt{3}) \\ 0.8/\mu & (\mu \geqslant \sqrt{3}). \end{cases} \tag{20}$$

This practical upper limit of λ is shown by the kinked solid curve in Fig. 4.

The numerical results from the analysis are expected to approach the exact values with increasing number of the boundary elements of the unit regions, N for the triangular region

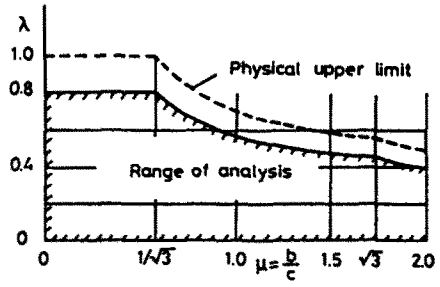

Fig. 4. Region of validity.

Table 1. Variations of results with number of subdivision ($\mu = 1$ and $\lambda = 0.5$, triangular region)

N	σ_{max}/σ	$\theta(deg)$	E^*/E_0
4	7.1485	16°	0.2133
8	7.0053	16°	0.2164
12	7.0047	17°	0.2164
16	7.0046	17°	0.2164
24	7.0046	17°	0.2164

or N_1 and N_2 for the rectangular region. As an example, Table 1 gives the results for the maximum stress, its location and the stiffness factor for the case of $\mu = 1$ and $\lambda = 0.5$, calculated by using the triangular unit region with 4, 8, 12, 16 and 24 boundary elements. We find rapid convergence of the numerical results with increasing values of N, and the errors seem to be less than 2% even when $N = 4$.

3.2. *Extreme cases when* c → ∞ *and* b → ∞

Consider the limiting cases when $c \to \infty$ and $b \to \infty$, which correspond to an infinite row of holes vertical and parallel to the loading direction as shown by Fig. 5(a) and (b), respectively. These problems were solved by Isida (1960) using a perturbation procedure, and have been reanalyzed here in order to get reliable results for wider ranges of $\lambda = a/b$ or $\lambda_1 = a/c$. Near exact values are obtained in the ranges of $\lambda, \lambda_1 \leqslant 0.8$. In the former case, the form factor (stress concentration factor) α is based on the mean stress over the minimum section, or $\alpha = (1-\lambda)\sigma_{max}/\sigma$.

The analytical values for both problems are given in Table 2 in the columns marked "analysis". These results are then fitted to power series of λ or λ_1 by using a least-square method, and the following formulae are obtained.

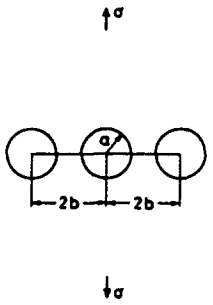

Fig. 5(a). Infinite row of circular holes under transverse tension.

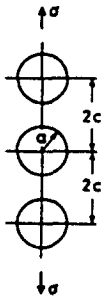

Fig. 5(b). Infinite row of circular holes under longitudinal tension.

Table 2. Infinite row of circular holes under uniaxial tension

Case	Transverse tension (Fig. 5(a))				Longitudinal tension (Fig. 5(b))	
λ	σ_{max}/σ		α		σ_{max}/σ	
λ_1	Analysis	Eqn.(21)	Analysis	Eqn.(22)	Analysis	Eqn.(23)
0	3.0	3.0	3.0	3.0	3.0	3.0
0.05	3.000	3.000	2.850	2.850	2.984	2.984
0.10	3.000	3.000	2.700	2.700	2.936	2.937
0.15	3.002	3.002	2.552	2.552	2.862	2.863
0.20	3.006	3.006	2.405	2.405	2.768	2.769
0.25	3.015	3.014	2.261	2.261	2.660	2.661
0.30	3.031	3.030	2.122	2.121	2.547	2.546
0.35	3.056	3.056	1.986	1.986	2.434	2.430
0.40	3.096	3.097	1.858	1.858	2.326	2.320
0.45	3.155	3.158	1.735	1.737	2.227	2.220
0.50	3.241	3.249	1.621	1.625	2.139	2.134
0.55	3.366	3.380	1.515	1.521	2.062	2.063
0.60	3.546	3.566	1.418	1.426	1.995	2.005
0.65	3.811	3.833	1.334	1.342	1.937	1.955
0.70	4.204	4.220	1.261	1.266	1.887	1.904
0.75	4.803	4.800	1.201	1.200	1.842	1.840
0.80	5.756	5.715	1.151	1.143	1.788	1.746
1.0	∞	∞	1.0	1.0		

Case (a): an infinite row of holes in the x-direction ($c \to \infty$)

$$\frac{\sigma_{max}}{\sigma} = \frac{1}{1-\lambda} + 2 - \lambda - \lambda^2 - \lambda^3 + 2.583\lambda^4 - 1.193\lambda^5 \tag{21}$$

$$\alpha = (1-\lambda)\frac{\sigma_{max}}{\sigma} \quad \text{(mean error = 0.2\%)}. \tag{22}$$

Case (b): an infinite row of holes in the y-direction ($b \to \infty$)

$$\frac{\sigma_{max}}{\sigma} = 3 - 6.687\lambda_1^3 + 1.961\lambda_1^3 + 15.715\lambda_1^4 - 13.476\lambda_1^5 \quad \text{(mean error = 0.3\%)}. \tag{23}$$

The values from eqns (21)–(23) are also given in Table 2, and show excellent agreement with the analytical values in the range of λ, $\lambda_1 \leqslant 0.8$.

3.3. *Circumferential stress and stress concentration factors*

3.3.1. *Effects of parameters on circumferential stress.* Figure 6(a–c) shows the distributions of the normalized circumferential stress σ_θ/σ for $c/b = 2$, 1 and 0.5. For large values of c/b [Fig. 6(a)], the stress distribution is similar to that for a horizontal row of holes, as shown by Fig. 5(a), and σ_{max} occurs at the point A ($\theta = 0$). When c/b is small [Fig. 6(c)], vertical rows of holes disturb the stress flow around the mid-portions of the sections between horizontally adjacent holes, and σ_{max} also takes place at point A.

For intermediate values of c/b [Fig. 6(b)], however, the situation is quite different. In such cases, σ_{max} occurs at point A for small values of λ, but as λ increases the stress flow around point A is considerably disturbed by the presence of obliquely located holes, and σ_{max} takes place at some other point B ($\theta \neq 0$). Usually we have the only peak value of σ_θ at A or B, but in a limited range of μ and for extremely large values of λ, two peak values are sometimes observed at points A and B, referred to again in the discussion of Fig. 8. Near exact values of σ_{max} have been obtained by calculating σ_θ at one degree intervals and taking their largest values. The above observations are different from previous papers by Saito (1957) and Bailey and Hicks (1960), in which the maximum stress was arbitrarily assumed to occur at point A.

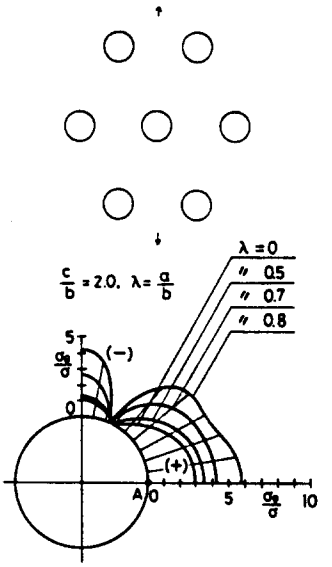

Fig. 6(a). Distribution of σ_θ/σ ($c/b = 2$).

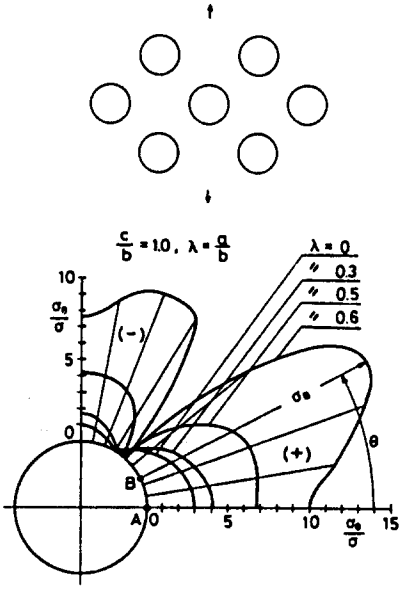

Fig. 6(b). Distribution of σ_θ/σ ($c/b = 1$).

Table 3 shows the numerical results of σ_A/σ for various values of μ and λ, together with the values of $\mu \to 0$ given in the second column of Table 2. In most of the calculated cases, σ_A gives the maximum circumferential stress, but not in the range bounded by the dotted line shown in the table. In this range, σ_{max} occurs at some other point B ($\theta \neq 0$), as shown in Fig. 6(b). The values of σ_B/σ ($= \sigma_{max}/\sigma$) and their locations θ (in degrees) are given in Table 4.

Figures 7 and 8 show the relations obtained between σ_{max}/σ and λ and between σ_{max}/σ and μ. We find that σ_{max}/σ increases rapidly with increasing values of μ or λ, due to the interference between adjacent holes. In a limited range of μ for large values of λ, two peak values sometimes take place at points A and B. The dashed curves in Fig. 8 show the lower peak value in such exceptional cases. On the curve for $\lambda = 0.8$ we notice a kink at $\mu_0 \doteqdot 0.53$ where $\sigma_A = \sigma_B$, and $\sigma_A > \sigma_B$ or $\sigma_A < \sigma_B$ depending whether $\mu < \mu_0$ or $\mu > \mu_0$, respectively.

3.3.2. *Stress concentration factors.* As shown in the preceding section, σ_A gives the maximum circumferential stress for a wide range of the parameters, where the form factor

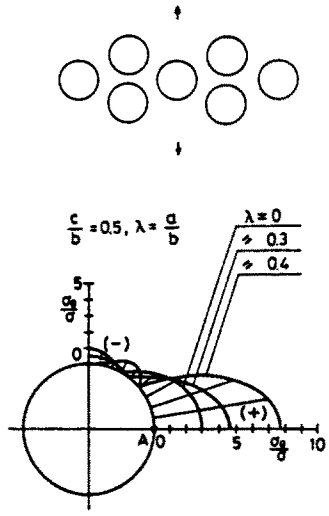

Fig. 6(c). Distribution of σ_θ/σ ($c/b = 0.5$).

Table 3. σ_A/σ

λ \ μ	0	0.25	0.33	0.4	0.5	$1/\sqrt{3}$	0.67	0.8	1.0	1.33	2.0
0.0	3.000	3.000	3.000	3.000	3.000	3.000	3.000	3.000	3.000	3.000	3.000
0.05	3.000	3.001	3.002	3.002	3.004	3.007	3.011	3.017	3.024	3.028	3.012
0.10	3.000	3.004	3.006	3.009	3.017	3.027	3.041	3.066	3.099	3.118	3.058
0.15	3.002	3.010	3.014	3.020	3.037	3.058	3.091	3.148	3.227	3.283	3.167
0.20	3.006	3.019	3.025	3.035	3.063	3.100	3.156	3.260	3.416	3.547	3.386
0.25	3.015	3.033	3.042	3.055	3.095	3.148	3.233	3.400	3.675	3.949	3.784
0.30	3.031	3.053	3.064	3.081	3.132	3.201	3.317	3.563	4.016	4.544	4.470
0.35	3.056	3.081	3.094	3.113	3.172	3.255	3.403	3.746	4.458	5.409	5.645
0.40	3.096	3.123	3.136	3.156	3.218	3.310	3.488	3.946	5.030	6.663	7.735
0.45	3.155	3.181	3.194	3.213	3.272	3.366	3.568	4.162	5.777	8.510	
0.50	3.241	3.265	3.277	3.291	3.340	3.428	3.645	4.398	6.770	11.38	
0.55	3.366	3.386	3.395	3.404	3.435	3.506	3.724	4.652	8.124		
0.60	3.546	3.562	3.567	3.569	3.576	3.618	3.815	4.914	10.02		
0.65	3.811	3.821	3.823	3.818	3.799	3.799	3.935	5.153			
0.70	4.204	4.209	4.208	4.198	4.156	4.106	4.129	5.326			
0.75	4.803	4.805	4.802	4.792	4.740	4.644					
0.80	5.756	5.756	5.754	5.747	5.707	5.600					

Table 4. σ_B/σ and their locations θ (deg)

λ \ μ	$1/\sqrt{3}$	0.67	0.8	1.0	1.33
0.50		3.645 (3°)	4.571 (19°)	7.005 (17°)	11.60 (13°)
0.55		3.902 (22°)	5.552 (26°)	9.628 (23°)	
0.60	3.650 (17°)	4.539 (29°)	7.413 (29°)	15.71 (27°)	
0.65	4.011 (27°)	5.703 (33°)	11.00 (32°)		
0.70	4.698 (34°)	7.764 (36°)	19.09 (35°)		
0.75	5.924 (38°)				
0.80	8.138 (41°)				

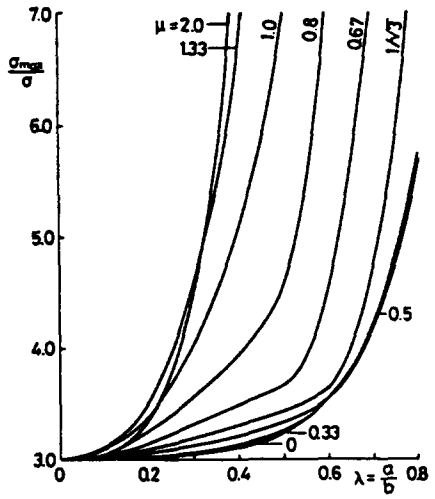

Fig. 7. Relations between σ_{max}/σ and λ for various μ.

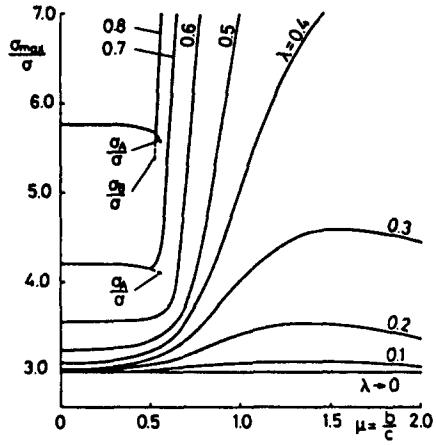

Fig. 8. Relations between σ_{max}/σ and μ for various λ.

(stress concentration factor) α_A is based on the mean stress over the minimum sections along the x-axis. Another form factor α_B is also defined from σ_B in the same manner as α_A:

$$\alpha_A = (1-\lambda)\frac{\sigma_A}{\sigma}, \quad \alpha_B = (1-\lambda)\frac{\sigma_B}{\sigma}. \tag{24}$$

The form factor α corresponding to the maximum stress is then defined as follows:

$$\alpha = \max(\alpha_A, \alpha_B). \tag{25}$$

Table 5 gives the values of α calculated from Tables 3 and 4 and eqns (24) and (25), where most of the values are α_A and the values below the dashed line are α_B.

The values of α are plotted by thick solid curves in Fig. 9. The thin solid curves in the figure show α_A in the range where $\alpha_A < \alpha_B$, occurring at λ around 0.45–0.5 for the calculated four cases of μ. When $\mu \leqslant 1/\sqrt{3}$, we have the limiting case $\lambda \to 1$ as shown by Fig. 3(a), where $\alpha_A \to 1$. If $\mu > 1/\sqrt{3}$, however, λ cannot exceed the value less than unity for the limiting cases as shown by Fig. 3(b) and (c). Triangular marks in Fig. 9 show the values of α_A for a square array given by Bailey and Hicks (1960) which have been estimated from diagrams in their paper. They are consistent with authors' α_A-curve for a wide range of $\lambda \leqslant 0.6$. Saito's results (1957), however, agree with the authors' only in the range of $\lambda \leqslant 0.15$, but not for larger values of λ.

Table 5. Stress concentration factor α

λ \ μ	0	0.25	0.33	0.4	0.5	$1/\sqrt{3}$	0.67	0.8	1.0	1.33	2.0
0.0	3.000	3.000	3.000	3.000	3.000	3.000	3.000	3.000	3.000	3.000	3.000
0.05	2.850	2.851	2.851	2.852	2.854	2.857	2.860	2.866	2.873	2.877	2.861
0.10	2.700	2.704	2.705	2.708	2.715	2.724	2.737	2.760	2.789	2.806	2.752
0.15	2.552	2.558	2.562	2.567	2.581	2.600	2.627	2.676	2.743	2.791	2.692
0.20	2.405	2.415	2.420	2.428	2.451	2.480	2.525	2.608	2.733	2.838	2.709
0.25	2.261	2.275	2.281	2.291	2.321	2.361	2.425	2.550	2.756	2.962	2.838
0.30	2.122	2.137	2.145	2.157	2.192	2.240	2.322	2.494	2.811	3.181	3.129
0.35	1.986	2.003	2.011	2.023	2.062	2.116	2.212	2.435	2.898	3.516	3.669
0.40	1.858	1.874	1.882	1.894	1.931	1.986	2.093	2.367	3.018	3.998	4.641
0.45	1.735	1.750	1.757	1.767	1.799	1.851	1.962	2.289	3.177	4.680	
0.50	1.621	1.633	1.638	1.646	1.670	1.714	1.823	2.286	3.502	5.800	
0.55	1.515	1.524	1.528	1.532	1.546	1.578	1.756	2.498	4.333		
0.60	1.419	1.425	1.427	1.428	1.431	1.460	1.816	2.965	6.285		
0.65	1.334	1.337	1.338	1.336	1.330	1.404	1.996	3.851			
0.70	1.261	1.263	1.262	1.259	1.247	1.409	2.329	5.726			
0.75	1.201	1.201	1.201	1.198	1.185	1.481					
0.80	1.151	1.151	1.151	1.149	1.141	1.628					

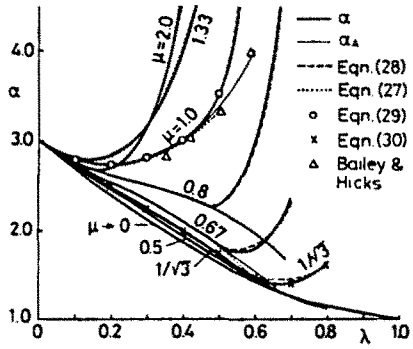

Fig. 9. Stress concentration factor α.

3.3.3. *Formulae for stress concentration factors.* In order to get reliable results for arbitrary values of the parameters μ and λ not covered in the 138 combinations studied, we have established power series formulae for α_A and α_B. Here the following aspects are taken into account.

(i) As shown in Fig. 9, the behavior of α_A depends on two ranges of μ: $\mu \leqslant 1/\sqrt{3}$ and $\mu > 1/\sqrt{3}$, and different formulae in the two ranges are expected to give better accuracy. We also refer to the limiting behavior as $(\alpha_A)_{\lambda\to 0} = 3$.

(ii) α_B should diverge when obliquely located holes touch each other, as shown in Fig. 3(b), or when λ approaches $\sqrt{1+\mu^2}/(2\mu)$.

Considering the above aspects, we have fitted power series involving μ and λ to the analytical values of α_A and α_B. The procedure is based on the least-square method, and the following formulae are obtained.

For α_A in the range $\mu \leqslant 1/\sqrt{3}$ and $\lambda \leqslant 0.8$:

$$\alpha_A = 1+(1-\lambda)(2-\lambda-\lambda^2-\lambda^3+2.583\lambda^4-1.193\lambda^5)$$
$$+(1-\lambda)\lambda^2\mu[-1.503+11.352\mu+\lambda(2.308-16.935\mu)] \quad \text{(mean error = 0.7\%)}. \quad (26)$$

For α_A in the range shown by hatched area for $\mu \geqslant 1/\sqrt{3}$ in Fig. 4:

$$\alpha_A = (1-\lambda)[3+\lambda^2(-2.874+2.996\mu+18.353\mu^2-8.817\mu^3)$$
$$+\lambda^3(-144.56+425.70\mu-386.37\mu^2+101.76\mu^3)$$
$$+\lambda^4(463.16-1469.3\mu+1395.0\mu^2-362.57\mu^3)] \quad \text{(mean error = 1.0\%)}. \quad (27)$$

For α_B in the range of μ and λ under the dashed line in Table 5:

$$\alpha_B = \frac{1-\lambda}{1-\dfrac{2\lambda\mu}{\sqrt{1+\mu^2}}}[19.866-84.068\mu+139.51\mu^2-67.482\mu^3$$
$$+\lambda(-78.877+385.05\mu-638.91\mu^2+308.61\mu^3)$$
$$+\lambda^2(104.01-504.07\mu+800.52\mu^2-375.33\mu^3)] \quad \text{(mean error = 1.3\%)}. \quad (28)$$

We are especially interested in the square array ($\mu = 1$) and the equilateral triangular array ($\mu = 1/\sqrt{3}$) shown in Fig. 10(a) and (b), respectively.

For these special cases, we have fitted polynomials for the total form factor α without separating it into α_A and α_B. They are the following equations (29) and (30), and give more accurate values than eqns (26)–(28).

Square array:

$$(\alpha)_{\mu=1} = (1-\lambda)\left[3+\frac{\lambda}{1-\sqrt{2}\lambda}(0.206+3.970\lambda+33.006\lambda^2-125.91\lambda^3+122.91\lambda^4)\right]$$
$$\text{(mean error = 0.3\%)}. \quad (29)$$

Equilateral triangular array:

$$(\alpha)_{\mu=1/\sqrt{3}} = (1-\lambda)\left[3+\frac{\lambda}{1-\lambda}(-0.009+2.801\lambda-2.160\lambda^2-10.633\lambda^3+14.404\lambda^4)\right]$$
$$\text{(mean error = 0.4\%)}. \quad (30)$$

Values from eqns (27)–(30) are plotted in Fig. 9 as dotted curves, dashed curves, open circles and crosses, respectively. Those from eqn (26) nearly coincide with the analytical values and are not shown in Fig. 9.

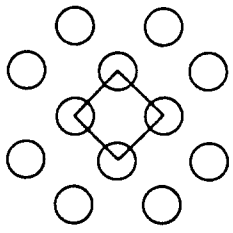

Fig. 10(a). Square array of holes ($\mu = 1$).

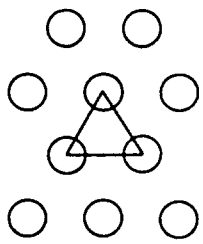

Fig. 10(b). Equilateral triangular array of holes ($\mu = 1/\sqrt{3}$).

Table 6. Tensile stiffness factor $C = E^*/E_0$ for various μ and λ

λ \ μ	0.25	0.33	0.5	$1/\sqrt{3}$	0.67	0.8	1.0	1.33	2.0
0.0	1.0	1.0	1.0	1.0	1.0	1.0	1.0	1.0	1.0
0.05	0.997	0.996	0.994	0.993	0.992	0.991	0.988	0.984	0.977
0.10	0.988	0.985	0.977	0.973	0.969	0.963	0.954	0.939	0.913
0.15	0.974	0.966	0.949	0.941	0.932	0.918	0.898	0.867	0.820
0.20	0.955	0.940	0.912	0.899	0.883	0.858	0.823	0.773	0.712
0.25	0.931	0.909	0.867	0.847	0.823	0.786	0.732	0.664	0.599
0.30	0.902	0.873	0.817	0.790	0.756	0.704	0.631	0.548	0.487
0.35	0.870	0.833	0.762	0.727	0.684	0.616	0.523	0.430	0.375
0.40	0.835	0.790	0.705	0.662	0.609	0.525	0.414	0.317	0.263
0.45	0.796	0.744	0.646	0.596	0.533	0.434	0.311	0.213	
0.50	0.755	0.696	0.586	0.529	0.457	0.345	0.216	0.124	
0.55	0.710	0.646	0.526	0.463	0.381	0.260	0.136		
0.60	0.663	0.594	0.466	0.397	0.308	0.182	0.072		
0.65	0.613	0.540	0.406	0.332	0.236	0.114			
0.70	0.559	0.485	0.347	0.268	0.168	0.059			
0.75	0.502	0.427	0.289	0.205					
0.80	0.440	0.368	0.232	0.146					

3.4. *Apparent tensile stiffness of perforated solid*

The apparent Young's modulus E^* of this perforated solid can be calculated from the displacement v at the point F in the case of the unit triangular region or from v at the point M in the case of the unit rectangular region (see Fig. 1).

Numerical results for the tensile stiffness factor C defined by eqns (19) are shown in Table 6 for various values of μ and λ and are plotted in Fig. 11. In the case of $\mu \to 0$, an infinite row of circular holes in the x-direction, C remains unity independent of λ, and it decreases considerably with increasing values of λ or μ. The curve for $\mu = 1$ (square array) is very close to that given by Bailey and Hicks (1960), shown by a dashed line.

Calculations have also been done for various values of μ and porosity f. The results are given in Table 7, and are plotted in Fig. 12, taking f as the abcissa instead of λ. We find that the C vs f curves in Fig. 12 lie in a narrower band than the C vs λ curves in Fig. 11. For better understanding, the results are replotted in Fig. 13 taking b/c as the abscissa. In this figure, C does not change monotonically with b/c, but it makes up-and-down fluctuations and takes the minimum around $\mu = 1$ for each value of f. This is the main reason why the curves in Fig. 12 lie within a narrow band.

The stiffness factor C is thus affected very little by the parameter μ, or by the distribution pattern of the holes, and it is nearly a function of the porosity only. A zig-zag array of circular holes may be regarded as a model of randomly distributed voids in solids. Therefore, the above observation seems to suggest a strong dependence of the tensile stiffness of actual solids on the porosity f.

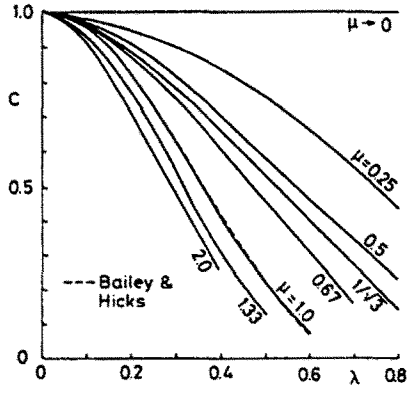

Fig. 11. C vs λ relations for various values of μ.

Table 7. Tensile stiffness factor $C = E^*/E_0$ for various μ and f

f \ μ	0.25	0.33	0.5	$1/\sqrt{3}$	0.67	0.8	1.0	1.33	2.0
0.0	1.0	1.0	1.0	1.0	1.0	1.0	1.0	1.0	1.0
0.05	0.866	0.866	0.865	0.864	0.862	0.859	0.857	0.859	0.867
0.10	0.751	0.756	0.754	0.750	0.744	0.734	0.728	0.734	0.759
0.15	0.645	0.661	0.661	0.653	0.642	0.624	0.611	0.624	0.670
0.20	0.544	0.575	0.580	0.570	0.553	0.527	0.508	0.527	0.594
0.25	0.443	0.495	0.509	0.496	0.474	0.441	0.417	0.441	0.527
0.30		0.419	0.444	0.430	0.404	0.365	0.337	0.365	0.467
0.35			0.385	0.369	0.340	0.297	0.268	0.298	0.411
0.40			0.331	0.313	0.281	0.237	0.208	0.239	0.360
0.45			0.281	0.262	0.228	0.185	0.158	0.187	0.311
0.50			0.235	0.214	0.180	0.139	0.116	0.143	0.266

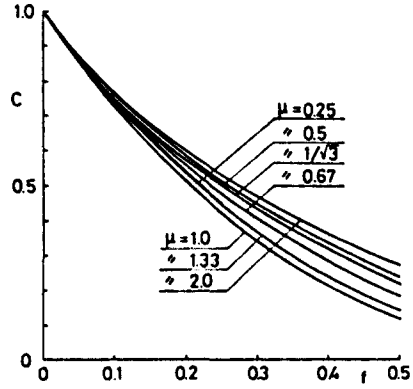

Fig. 12. C vs f relations for various values of μ.

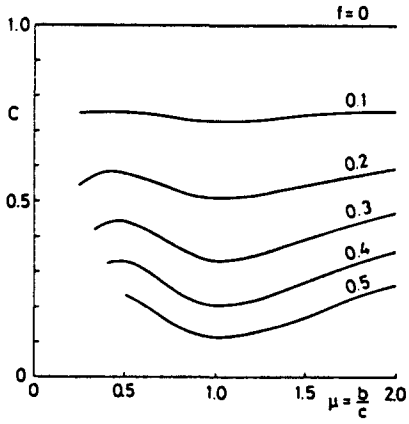

Fig. 13. C vs μ relations for various values of f.

Based on the above information, analytical values for C have been fitted to power series in μ and f,

$$C = 1 + f[-2.518 - 1.020f + 10.656f^2 + \mu(-1.082 + 17.983f - 45.345f^2) + \mu^2(0.739 - 19.150f + 45.710f^2) + \mu^3(-0.144 + 5.856f - 13.455f^2)]$$

(mean error = 2.9%). (31)

For the square and the equilateral triangular arrays shown in Fig. 10(a) and (b), we get the more reliable formulae

$$(C)_{\mu=1} = 1-2.998f+2.788f^2-0.380f^3-0.546f^4 \quad \text{(mean error = 0.01\%)} \tag{32}$$

$$(C)_{\mu=1/\sqrt{3}} = 1-2.988f+5.624f^2-8.306f^3+5.455f^4 \quad \text{(mean error = 0.1\%).} \tag{33}$$

4. CONCLUSIONS

(1) For small or large values of c/b, the maximum stress occurs at point A ($\theta = 0$) [Fig. 6(a) and (c)]. For intermediate values of c/b and large values of a/b, however, it takes place at point B($\theta \neq 0$) due to severe interactions between obliquely located holes [Fig. 6(b)]. Numerical values of the stress concentration factors are fitted to reliable polynomials (21)–(30).

(2) The tensile stiffness factor C of the solid is nearly a function of the porosity f and is independent of b/c in the range $0.25 \leqslant b/c \leqslant 2$. This observation seems to suggest a strong f-dependence of the tensile stiffness of actual solids with randomly distributed voids. Numerical results of C are fitted to reliable polynomials (31)–(33).

(3) For irregular distributions of holes, a general analysis on elliptical holes is available (Isida, 1973). Here the shapes, sizes, locations and orientations of the elliptical holes may be arbitrary. Circular inclusions and cracks may also be included. The current computer program is valid for less than 20 holes or cracks.

(4) The analytical concept based on element-wise resultant forces may be usefully applied to more realistic problems such as a regular distribution of spherical cavities.

REFERENCES

Bailey, R. and Hicks, R. (1960). Behaviour of perforated plates under plane stress. *J. Mech. Engng Sci.* **2**, 143.

Isida, M. (1960). On some plane problems of an infinite plate containing an infinite row of circular holes. *Bull. Jap. Soc. Mech. Engrs* **10**, 259.

Isida, M. (1971). Effect of width and length on stress intensity factors of internally cracked plates under various boundary conditions. *Int. J. Fracture Mech.* **7**, 301.

Isida, M. (1973). Method of Laurent series expansion for internal crack problems. In *Mechanics of Fracture* 1 (Edited by G. C. Sih), p. 56. Noordhoff, Leiden.

Isida, M. (1978). A new procedure of the body force method with applications to fracture mechanics. *Proc. 1st Int. Conf. Numer. Meth. Fracture Mech.*, Swansea, p. 81.

Isida, M. and Nemat-Nasser, S. (1987). A unified analysis of various problems relating to circular holes with edge cracks. *Engng Fracture Mech.* **27**, 571.

Isida, M. and Noguchi, H. (1984). Tension of a plate containing an embedded elliptical crack. *Engng Fracture Mech.* **20**, 387.

Isida, M., Tsuru, H. and Noguchi, H. (1983). New method of analysis of three dimensional crack problems. *Memoirs*, Vol. 43, p. 317. Faculty of Engineering, Kyushu University, Japan.

Isida, M. Noguchi, H. and Yoshida, T. (1984). Tension and bending of finite thickness plates with a semi-elliptical surface crack. *Int. J. Fracture* **26**, 157.

Saito, H. (1957). Stress in a plate containing infinite parallel rows of holes. *ZAMM* **37**, 111.

Timoshenko, S. and Goodier, J. N. (1951). *Theory of Elasticity*, 2nd Edn. McGraw-Hill, New York.